RSC Advances

PAPER

View Article Online
View Journal | View Issue

Cite this: *RSC Adv.*, 2026, **16**, 4275

Chalcogen substitution and ionization effects on the fluorescence behavior of 8-chalcogen-quinoline-BODIPY: a DFT and TD-DFT investigation

Mai Van Bay,[a] Quan V. Vo,[b] Nguyen Quang Trung,[c] Nguyen Linh Nam,[b] Pham Cam Nam[d] and Nguyen Minh Thong*[a]

Chalcogen substitution and ionization provide effective routes for tuning the photophysical properties of BODIPY-based fluorophores, yet their combined impact on excited-state proton and charge transfer remains insufficiently understood. Herein, density functional theory (DFT) and time-dependent DFT (TD-DFT) calculations are employed to systematically investigate the effects of chalcogen replacement (O, S, Se) and protonation/deprotonation on the electronic structure and fluorescence behavior of 8-chalcogen-quinoline-BODIPY (8QBDY-X, X = O, S, Se) derivatives. The results reveal that heavier chalcogens enhance π-delocalization and excited-state polarizability while weakening the ground-state intramolecular hydrogen bond and facilitating excited-state intramolecular proton transfer. Frontier molecular orbital, molecular electrostatic potential, dipole moment, Wiberg bond index, and NBO/AIM analyses consistently demonstrate that protonation stabilizes localized excited states with large electronic and optical gaps, whereas deprotonation narrows these gaps and activates photoinduced electron transfer or intramolecular charge transfer pathways. Optical band gap and exciton binding energy analyses further show reduced electron–hole binding in the deprotonated sulfur- and selenium-substituted derivatives, rationalizing their red-shifted and tunable emission. Notably, the computed excited-state characteristics of 8QBDY-O are qualitatively consistent with the experimentally observed ON/OFF fluorescence switching upon protonation/deprotonation. These findings provide mechanistic insight and design guidelines for BODIPY-based fluorescent sensors.

Received 26th November 2025
Accepted 13th January 2026

DOI: 10.1039/d5ra09145d

rsc.li/rsc-advances

1. Introduction

Excited-state intramolecular proton transfer (ESIPT) and photoinduced electron transfer (PeT) are two fundamental photophysical processes that play central roles in modulating the fluorescence properties of organic fluorophores and molecular sensors.[1–4] Molecules capable of ESIPT typically exhibit large Stokes shifts,[5–7] and dual-emission features,[8] making them valuable for applications in bioimaging,[9] optoelectronics,[10] and luminescent materials.[11] Similarly, PeT-based systems are of great importance for designing molecular switches and fluorescence "ON/OFF" sensors, where protonation or electronic perturbation regulates charge transfer between donor and acceptor fragments.[3,4,12] The interplay between these two excited-state pathways provides a versatile framework for tailoring the fluorescence response of functional dyes.

Among fluorophore scaffolds, Boron-dipyrromethene (BODIPY) dyes have emerged as one of the most versatile families of fluorophores owing to their exceptional photostability, high fluorescence quantum yields, sharp absorption/emission bands, and structural tunability through synthetic modifications.[13,14] Their rigid π-conjugated framework and chemical robustness make BODIPY derivatives attractive for applications in fluorescence sensing, bioimaging, and optoelectronic devices.[15] Moreover, the BODIPY core offers extensive opportunities for fine-tuning its photophysical behavior by conjugation with heteroaromatic systems, which can introduce additional charge-transfer or proton-transfer functionalities.

Recent studies have further demonstrated that heteroatom substitution and peripheral functionalization play a decisive role in regulating excited-state relaxation pathways, fluorescence efficiency, and charge-transfer character in conjugated fluorophores.[16–22] Among various structural modifications, the conjugation of BODIPY with heteroaromatic systems such as 8-hydroxyquinoline has proven particularly promising. Previous studies have revealed that 8-hydroxyquinoline-BODIPY hybrid systems exhibit either ON/OFF or OFF-ON-OFF fluorescence

[a]The University of Danang – University of Sciences and Education, Danang 550000, Vietnam. E-mail: nmthong@ued.udn.vn
[b]The University of Danang – University of Technology and Education, Danang 550000, Vietnam
[c]Quality Assurance and Testing Center 2, Da Nang 550000, Vietnam
[d]The University of Danang - University of Technology and Sciences, Danang 550000, Vietnam

switching behavior, driven by photoinduced electron transfer (PeT) modulation under acidic and basic conditions.[23,24] These dual-mode sensors are particularly valuable for distinguishing protonation states and microenvironmental polarity, enabling fine control over fluorescence output in diverse media.

Although the excited-state intramolecular proton transfer (ESIPT) process of 8-hydroxyquinoline has been extensively studied,[25] it remains unclear whether a similar ESIPT process occurs in the 8-hydroxyquinoline-BODIPY system. Traditionally, ESIPT has been associated with O–H···N type hydrogen bonds.[26,27] However, Pi-Tai Chou and co-workers recently provided the first experimental evidence of an S–H-type ESIPT occurring at room temperature in a 3-thioflavone system,[28] thereby suggesting that heavier chalcogen analogues (*e.g.*, Se–H) may also participate in ESIPT phenomena.

From a fluorescence-sensor design perspective, it is essential to clarify how the replacement of oxygen with heavier chalcogens such as sulfur or selenium in 8-chalcogen-quinoline-BODIPY derivatives (abbreviated as 8QBDY-X, X = O, S, Se) affects the excited-state intramolecular proton transfer (ESIPT) process. Furthermore, elucidating whether the protonated (cationic) and deprotonated (anionic) forms of 8QBDY-S and 8QBDY-Se exhibit pH-dependent fluorescence behavior similar to that of 8QBDY-O is of particular significance. A comprehensive understanding of these aspects will deepen insight into the fluorescence mechanisms of chalcogen-quinoline-BODIPY systems and provide a foundation for the rational design of next-generation fluorescent materials with tunable structure-environment-ionization relationships.

Computational chemistry provides a powerful platform for exploring these mechanisms at the molecular level. Quantum chemical methods, particularly those based on density functional theory (DFT) and time-dependent DFT (TD-DFT), enable accurate modeling of ground and excited-state geometries, electronic transitions, and potential energy surfaces of ESIPT processes.[29–31] Through these approaches, one can disentangle the interplay between chalcogen substitution, protonation state, and electronic coupling in determining the photophysical response of BODIPY-based fluorophores.

Previous studies on chalcogen-substituted quinoline derivatives have revealed that heteroatom identity and ionization state influence photophysical behavior. Anderson and Hercules showed that 8-mercaptoquinoline exhibits a visible absorption at 549 nm and emission at 406 nm in acetonitrile,[32] attributed to a zwitterionic charge-transfer transition and S_2-state fluorescence. The pronounced solvent dependence and quenching in protic media indicate that protonation equilibria and intramolecular charge transfer govern its photophysical behavior. Complementary crystallographic analyses by Silin *et al.* demonstrated that Hg(8-hydroxyquinolinate)$_2$, Hg(8-mercaptoquinolinate)$_2$, and Hg(8-selenolquinolinate)$_2$ are isostructural, with Hg–E bond distances increasing from O → S → Se, accompanied by enhanced covalency and electronic polarizability.[33] These findings confirm that heavier chalcogens facilitate orbital delocalization and electron-donor softness, thereby stabilizing charge-transfer states. Collectively, these observations suggest that both chalcogen substitution and ionization state play decisive roles in modulating ESIPT and PeT pathways in quinoline-based fluorophores.

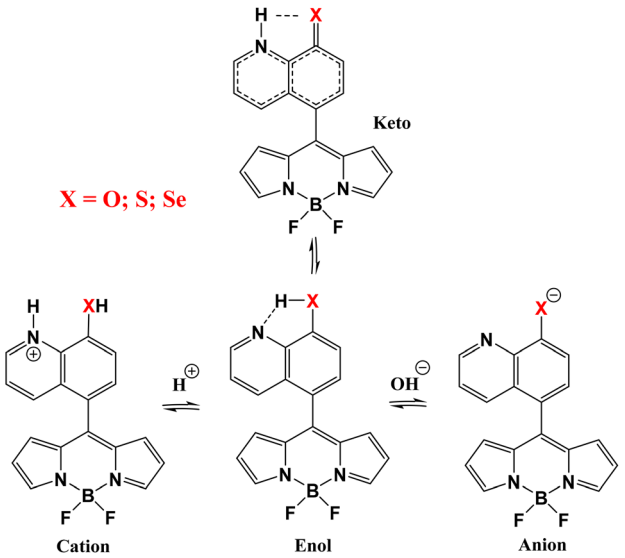

Fig. 1 Structures of 8-chalcogen-quinoline-BODIPY (8QBDY-X) derivatives.

Building on these insights, the present study employs computational methods to systematically investigate the influence of chalcogen substitution (X = O, S, Se) and protonation/deprotonation states on the fluorescence properties and ESIPT/PeT mechanisms of 8-chalcogen-quinoline-BODIPY (8QBDY-X, X = O, S, Se) derivatives (Fig. 1). The results are expected to offer fundamental insights into structure–property relationships and provide theoretical guidance for the rational development of BODIPY-quinoline-based fluorescent probes with tunable structural, electronic, and environmental responsiveness.

2. Computational methods

All quantum chemical calculations were performed using Density Functional Theory (DFT) and Time-Dependent DFT (TD-DFT) methods as implemented in the Gaussian 16 software package.[34] Geometry optimizations of the ground (S_0) and first excited (S_1) states of 8-chalcogen-quinoline-BODIPY derivatives were carried out at the ωB97X-D/6-311G(d,p) level of theory. The ωB97X-D functional was chosen for its balanced treatment of long-range exchange and dispersion interactions, offering reliable performance for π-conjugated and BODIPY-type systems.[31]

Harmonic vibrational frequency analyses were performed at the same level to verify that all optimized structures correspond to true minima (no imaginary frequencies). To account for solvent effects, the conductor-like polarizable continuum model (CPCM) was employed,[35] with acetonitrile chosen as the solvent to mimic experimental conditions.[23,24]

Potential energy surfaces (PES) for the excited-state intramolecular proton transfer (ESIPT) reactions were obtained by performing relaxed potential energy scans along the X–H coordinate in the S_1 state. The reaction rate constants (k) were

calculated using conventional transition-state theory (TST) according to:

$$k = \frac{k_B T}{h} \exp\left(-\frac{\Delta G^{\ddagger}}{RT} \right)$$

where k_B is the Boltzmann constant, T is the absolute temperature, h is the Planck constant, R is the gas constant, and $\Delta G^{\ddagger}$ denotes the Gibbs free energy of activation.

Each transition state (TS) structure was confirmed to exhibit exactly one imaginary frequency corresponding to the X–H···N proton-transfer coordinate. Intrinsic reaction coordinate (IRC) calculations were performed in both forward and reverse directions to ensure that each TS correctly connects the associated enol and keto minima on the potential energy surface.

Electronic structure analyses were performed on the optimized geometries at the ωB97X-D/6-311G(d,p) level of theory.

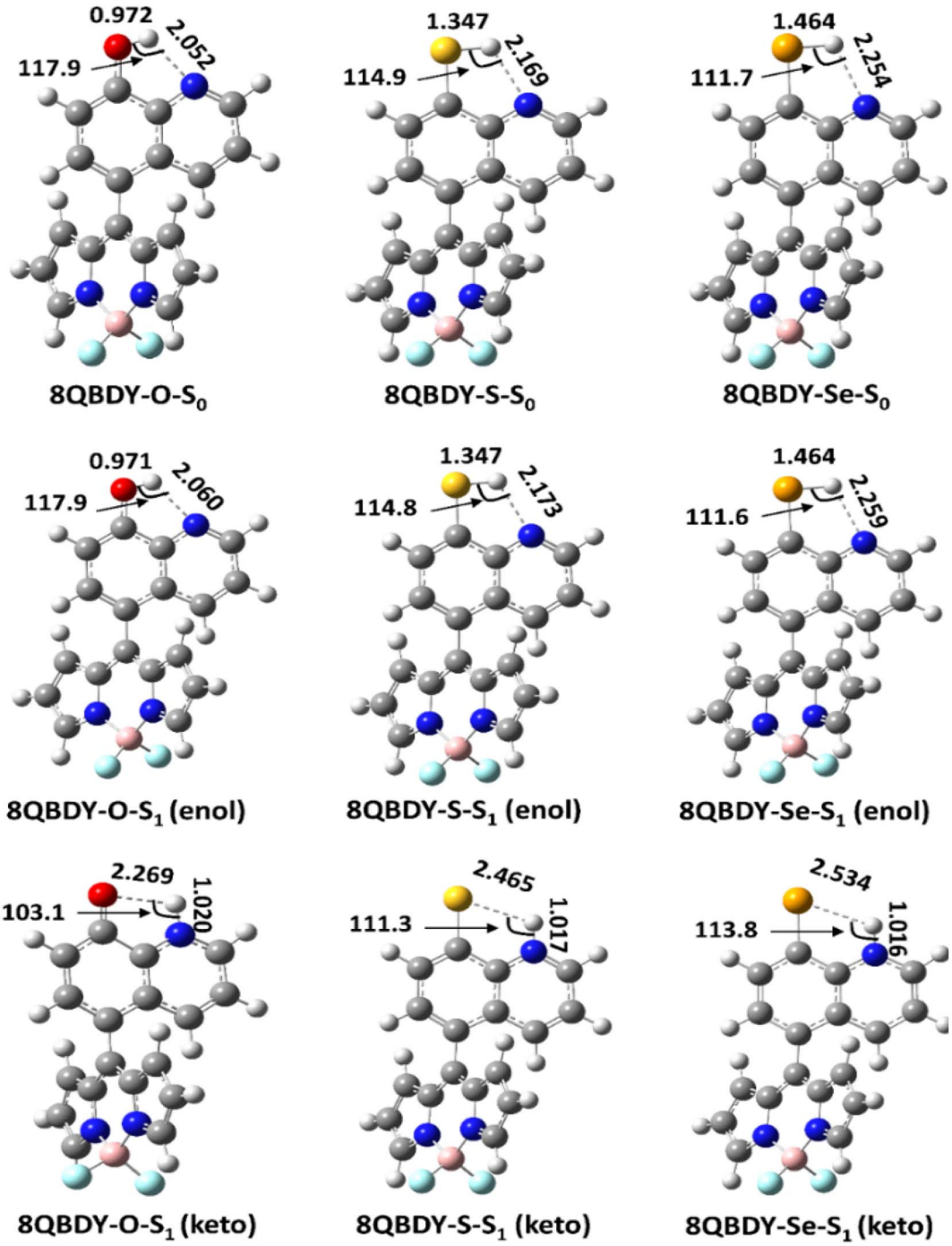

Fig. 2 The optimized geometrical parameters of the neutral 8-chalcogen-quinoline-BODIPY derivatives (8QBDY-X, X = O, S, Se) in both the ground (S_0) and first excited (S_1) states.

Molecular electrostatic potential (MEP) maps were generated on the ground-state electron density isosurface (ρ = 0.001 a.u), while bonding characteristics were examined using quantum theory of atoms in molecules (QTAIM) and natural bond orbital (NBO) analyses. The electronic band gap (E_g) was estimated from the HOMO–LUMO energy difference, and the optical band gap (E_{opt}) was obtained from the lowest vertical excitation energy calculated using TD-DFT.[36–38] The exciton binding energy was evaluated as $E_b = E_g - E_{opt}$. Dipole moments were calculated for both ground (S_0) and excited (S_1) states, and the dipole moment change ($\Delta\mu$) was used to assess photoinduced charge redistribution.

The Cartesian coordinates and energies of all investigated compounds are provided in the SI.

3. Results and discussion

3.1. Structural and spectroscopic properties of neutral forms

3.1.1. Electron structure characteristics, electrostatic potential surface (MEP) and dipole moment analysis. The replacement of oxygen by heavier chalcogens (S, Se) in the 8-chalcogen-quinoline-BODIPY series induces systematic alterations in bonding characteristics that govern the ESIPT reactivity. As presented in Fig. 2, the X–H bond length increases sequentially from 0.972 Å (O–H) to 1.347 Å (S–H) and 1.464 Å (Se–H), consistent with the periodic decrease in electronegativity and increase in atomic radius from oxygen to selenium. The lower electronegativity and higher covalency of sulfur and selenium result in a weaker and less polar X–H bond compared with the O–H bond. S–H type ESIPT occurs at room temperature, confirming that the excited-state polarization of the thiol moiety can overcome its intrinsically weak ground-state hydrogen bonding.[28] Consequently, the ESIPT propensity is enhanced along the O → S → Se sequence, with the Se–H bond exhibiting the highest polarizability and thus the greatest tendency for proton transfer. In the keto* forms of the S_1 state, the newly formed N–H bonds are progressively shorter, 1.020 Å for O, 1.017 Å for S, and 1.016 Å for Se, indicating a stronger N–H interaction and reinforcing the stabilization of the keto* tautomer in the excited state. Overall, the decreasing electronegativity and increasing atomic size of the chalcogen centers facilitate proton mobility, leading to more efficient photo-tautomerization from oxygen to selenium analogs.

As shown in Fig. S1 of SI, the molecular electrostatic potential (MEP) surfaces calculated for the ground state (S_0) showed that pronounced negative potential regions (red) are localized around the nitrogen atom, identifying it as the primary proton-accepting site, whereas positive potential regions (blue) are mainly distributed around the hydrogen atom bonded to the chalcogen atom (X–H), consistent with its proton-donating role. Upon replacing oxygen with heavier chalcogens (S and Se), the MEP distribution becomes less polarized around the X–H bond, reflecting the reduced electronegativity of the chalcogen atom and the weaker polarization of the X–H bond.

Dipole moment analysis further supports the electronic effects induced by chalcogen substitution and photoexcitation. As shown in Table S1 of SI, the ground-state (S_0) enol forms display a gradual decrease in dipole moment from 5.046 D (O) to 3.654 D (S) and 3.566 D (Se), reflecting the reduced polarity of the X–H bond upon replacement of oxygen by heavier chalcogens, consistent with the MEP results. Upon excitation to the S_1 state, the enol forms exhibit only minor dipole moment changes ($\Delta\mu$ = −0.147 to −0.029 D), indicating negligible charge redistribution prior to proton transfer. In contrast, the keto* forms in the S_1 state show a pronounced increase in dipole moment, reaching 10.315, 8.761, and 8.699 D for O, S, and Se derivatives, respectively, corresponding to large positive $\Delta\mu$ values of 5.107–5.269 D. This substantial enhancement arises from ESIPT-induced charge redistribution following proton transfer to the nitrogen atom.

3.1.2. Infrared (IR) vibrational spectra analysis. The calculated IR spectra of neutral 8QBDY–X derivatives (X = O, S, Se) in both S_0 and S_1 states (Fig. 3) reveal systematic chalcogen-dependent variations in X–H stretching vibrations. The O–H stretching vibration is located at 3685 cm^{-1}, which is characteristic of free phenolic O–H groups.[39,40] In contrast, the S–H and Se–H stretching modes appear at significantly lower frequencies, 2676 cm^{-1} and 2468 cm^{-1}, respectively, consistent with literature reports for thiol and selenol functionalities.[41–45] The progressive red shift from O–H to S–H and Se–H reflects the

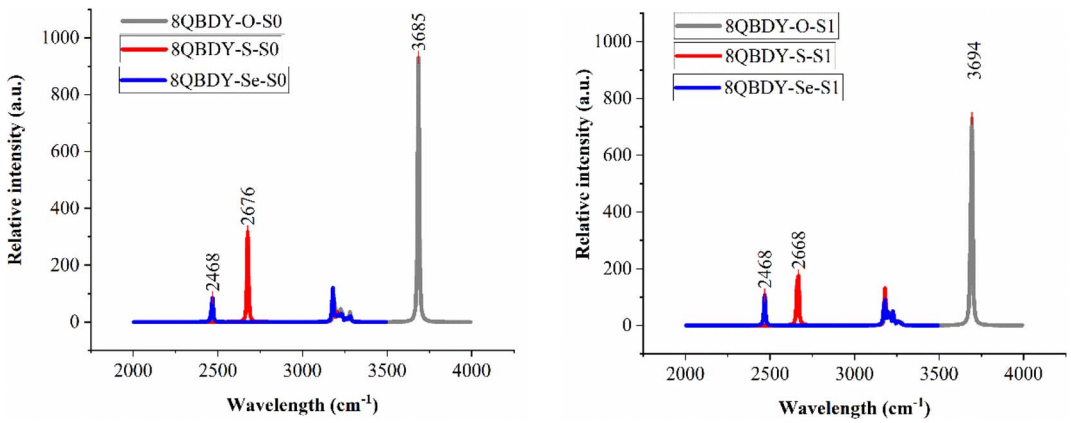

Fig. 3 Calculated IR spectra for X–H stretching vibrations of neutral 8QBDY–X derivatives (X = O, S, Se) in S_0 and S_1 states.

increasing atomic mass and decreasing bond force constant along the chalcogen series.[42] Concomitantly, the IR intensities of the ν(X–H) bands decrease markedly from O–H to Se–H, in line with previous spectroscopic analyses indicating reduced dipole moment derivatives and weaker X–H bonds for heavier chalcogens.[42,44] For the excitation state, minimal frequency changes are observed. The O–H mode slightly blue-shifts (3685–3694 cm^{-1}), while S–H and Se–H remain nearly constant, consistent with negligible structural variation between S_0 and S_1.

3.1.3. Potential energy surfaces and kinetic analysis of ESIPT processes. Flexible potential energy surface (PES) scanning was performed by systematically varying the X–H bond length (X = O, S, Se) while optimizing all other geometric parameters at each scan point. The obtained results of the potential energy profiles are illustrated in Fig. 4.

Across both electronic states, a consistent trend is observed, the energy barriers for the enol → keto transitions decrease progressively as the chalcogen atom becomes heavier (O → S → Se). Specifically, the forward barrier heights are 16.84, 8.34, and 6.79 kcal mol^{-1} in the S_0 state, and 15.52, 8.40, and 6.80 kcal mol^{-1} in the S_1 state for 8QBDY-O, 8QBDY-S, and 8QBDY-Se, respectively. The close similarity between the S_0 and S_1 barriers indicates that photoexcitation does not drastically alter the potential energy landscape, although it slightly stabilizes the keto* configuration and facilitates proton transfer.

The systematic reduction in barrier height from oxygen to selenium can be rationalized by the increasing atomic polarizability and enhanced electron delocalization capacity of sulfur and selenium. These effects weaken the X–H bond while simultaneously strengthening the intramolecular N···H interaction, thereby lowering the activation energy for proton migration. Consequently, 8QBDY-S and 8QBDY-Se display more favorable proton-transfer energetics than the oxygen analogue, indicating that chalcogen substitution exerts a key electronic influence on the modulation of ESIPT barriers and excited-state photodynamics in BODIPY-based fluorophores.

The kinetic parameters of the ESIPT reactions were evaluated from the calculated Gibbs free energies of activation ($\Delta G^{\ddagger}$) and rate constants (k) in the S_1 state (Table 1). A clear trend is observed in which the ESIPT rate increases systematically from oxygen to selenium substitution. For 8QBDY–O, $\Delta G^{\ddagger}$ is 13.54 kcal mol^{-1} with a rate constant of 7.39×10^2 s^{-1}, reflecting a rigid O–H···N hydrogen bond and slow proton migration. In contrast, 8QBDY–S exhibits a reduced $\Delta G^{\ddagger}$ of 7.81 kcal mol^{-1} and a faster rate of 1.17×10^7 s^{-1}, while 8QBDY–Se shows the lowest barrier (6.89 kcal mol^{-1}) and the highest rate (5.53×10^7 s^{-1}).

Table 1 Gibbs free energy of activation $\Delta G^{\ddagger}$ and rate constant (k) of the ESIPT process of the studied compounds in the excited state S_1

Compounds	$\Delta G^{\ddagger}$ (kcal mol^{-1})	k (s^{-1})
8QBDY-O	13.54	7.39×10^2
8QBDY-S	7.81	1.17×10^7
8QBDY-Se	6.89	5.53×10^7

Although ESIPT barriers and TST rate constants were calculated for all derivatives, the actual population of the keto state depends on the competition between ESIPT and excited-state decay processes. In the Se derivative, the substantially lower S_1 barrier leads to an ESIPT rate that is orders of magnitude higher than those of the O and S analogues, making it competitive with typical excited-state lifetimes. As a result, only the Se derivative is expected to accumulate a significant keto* population, whereas for O and S derivatives, ESIPT remains kinetically hindered.

The optimized structures and corresponding imaginary frequencies of each transition state for the ESIPT process are presented in Fig. 5. The corresponding IRC profiles (Fig. S2 of SI) further substantiate that each transition state represents a genuine first-order saddle point for the ESIPT pathway.

The progressive decrease in $\Delta G^{\ddagger}$ and increase in k along the O → S → Se series highlight the crucial role of chalcogen polarizability and electronic delocalization. These effects weaken the X–H bond, strengthen intramolecular N···H interactions, and stabilize the transition state, thereby promoting faster and more efficient ESIPT dynamics in the heavier chalcogen derivatives.

3.1.4. Absorption and emission properties. The TD-DFT calculated absorption and fluorescence spectra of 8QBDY-O, 8QBDY-S, and 8QBDY-Se (Table 2 and Fig. S3) exhibit distinct chalcogen-dependent photophysical behaviors. The lowest-

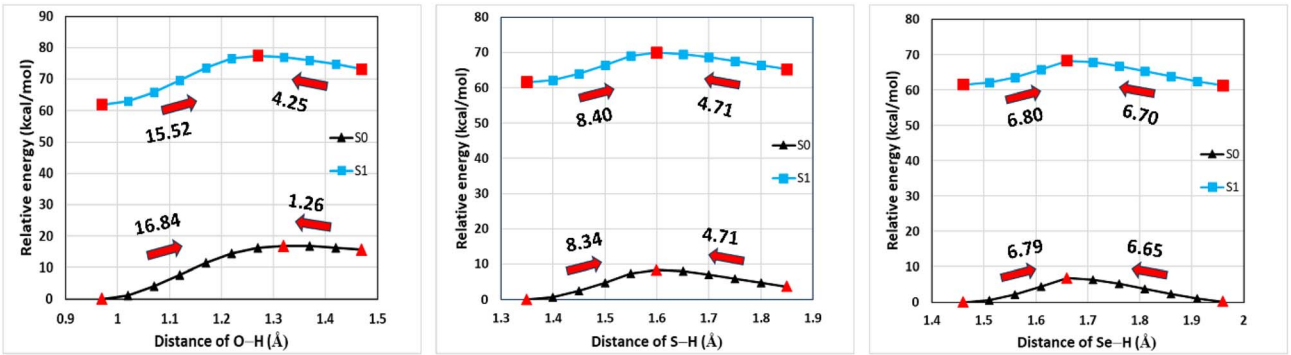

Fig. 4 Scanned potential energy curves of ground (S_0) and excited (S_1) states for the studied compound.

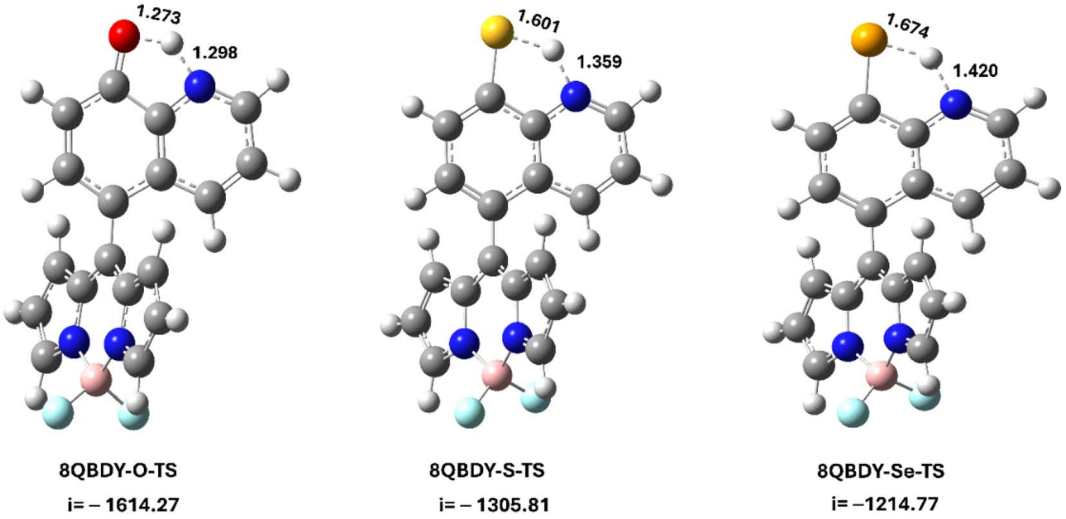

Fig. 5 The optimized transition state structures of investigated compounds for the ESIPT process in the excited state S_1, i – imaginary frequency.

energy absorption bands of the neutral 8QBDY–X derivatives (418–419 nm) are therefore attributed to the intrinsic BODIPY-centered π–π* (HOMO→LUMO) transition, which is known to exhibit large oscillator strengths and minimal sensitivity to meso-substitution.[15,46] Previous experimental and theoretical studies have consistently shown that quinoline or 8-hydroxyquinoline substituents predominantly affect excited-state deactivation pathways rather than the nature of the primary absorption transition.[23,47]

For 8QBDY-O, the enol emission occurs at 471 nm (f = 0.6988) with a moderate Stokes shift of 53 nm, while the keto form remains non-emissive. In 8QBDY–S, the enol* band is observed at 457 nm (f = 0.7453), and a weak keto* emission emerges at 480 nm (f = 0.2577), suggesting partial ESIPT activity. The selenium analogue exhibits the strongest dual-emission character, with enol* and keto* emissions at 474 nm (f = 0.7042) and 607 nm (f = 0.4949), corresponding to a large Stokes shift of 188 nm.

The red shift of the keto* emission upon replacing oxygen with heavier chalcogens can be rationalized by the decreasing electronegativity of the chalcogen atom, which enhances electronic delocalization and preferentially stabilizes the keto excited state. Similar chalcogen-dependent red-shift trends have been reported for other fluorophores.[16,48–50]

These results suggest that heavier chalcogen atoms enhance charge delocalization and intramolecular charge-transfer (ICT) character, stabilize the keto* state, and promote efficient ESIPT, leading to red-shifted and dual fluorescence in 8QBDY-based systems.

Table 2 The absorption and fluorescence spectra of neutral 8QBDY-O, 8QBDY-S and 8QBDY-Se

Compounds	$\lambda_{Abs.}$ (nm)	f (oscillator strengths)	$\lambda_{Flu.}$ (nm)	f (oscillator strengths)	Stokes shifts
8QBDY-*O*-enol	418	0.5247	471	0.6988	53
8QBDY-*O*-keto			OFF		
8QBDY-*S*-enol	419	0.5427	457	0.7453	38
8QBDY-*S*-keto			480	0.2577	61
8QBDY-Se-enol	419	0.5438	474	0.7042	55
8QBDY-Se-keto			607	0.4949	188

3.1.5. Frontier molecular orbitals (MOs), optical band gap (E_{opt}) and exciton binding energy (E_b) analysis. The frontier molecular orbitals of 8QBDY-O, 8QBDY-S, and 8QBDY-Se were analyzed to elucidate how chalcogen substitution affects the electronic structure and optical transitions. In the absorption states, the calculated HOMO and LUMO energies (Fig. 6) reveal a gradual reduction in the HOMO–LUMO gap from 6.43 eV (O) to 6.40 eV (S) and 6.34 eV (Se), indicating a systematic narrowing of the electronic band gap as the chalcogen atom becomes heavier. This effect originates from the increased orbital diffuseness and polarizability of sulfur and selenium, which strengthen π-conjugation and promote intramolecular charge transfer (ICT) within the quinoline-BODIPY scaffold.

In the excited (emissive) states, similar tendencies are observed, with smaller energy gaps for the keto tautomers (5.31–

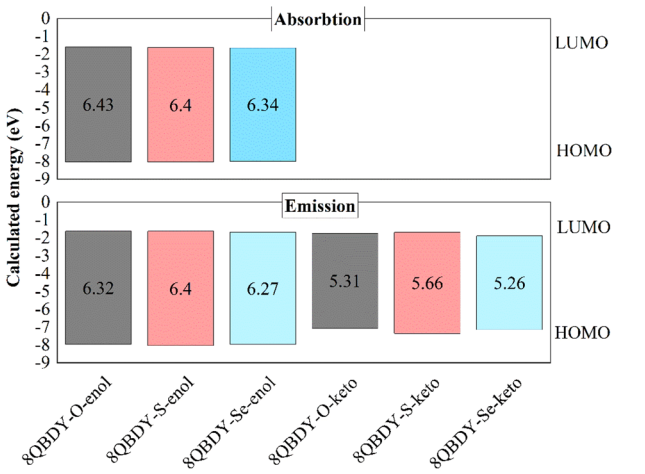

Fig. 6 Energy diagram of HOMO and LUMO levels of absorption/emission of neutral form of 8QBDY-O, 8QBDY-S and 8QBDY-Se.

5.26 eV) compared with the enol species. The reduced gaps reflect stronger charge delocalization and higher electronic softness, consistent with the predicted red-shifted emissions and enhanced ESIPT activity. Frontier orbital visualizations (Fig. 7) further show that the HOMOs are mainly distributed over the quinoline and BODIPY π-frameworks, whereas the LUMOs are localized on the BODIPY core, indicating dominant π → π* transitions with partial ICT character.

In general, the progressive decrease in the HOMO–LUMO gap from O → S → Se highlights the role of chalcogen substitution in stabilizing the excited keto state and enhancing charge-transfer efficiency, which is further reflected in the optical band gap (E_{opt}) and exciton binding energy (E_b) characteristics. As shown in Table S2 of SI, the enol forms exhibit E_{opt} values within a narrow range of 2.61–2.71 eV, indicating that vertical optical excitation in the enol configuration is only weakly influenced by chalcogen substitution. In contrast, the keto tautomers display markedly reduced E_{opt} values, particularly for 8QBDY-*O*-keto (1.80 eV) and 8QBDY-Se-keto (2.04 eV), reflecting substantial optical gap narrowing upon ESIPT and consistent with the red-shifted emission of the keto* species. The exciton binding energies provide complementary insight into electron–hole interactions: the enol forms show relatively large E_b values of 3.66–3.69 eV, characteristic of localized excitations, whereas the keto* forms exhibit reduced E_b values of 3.51 eV (O), 3.08 eV (S), and 3.22 eV (Se), indicating weakened electron–hole attraction due to enhanced charge delocalization and partial intramolecular charge-transfer character in the excited state. Notably, the lower E_b values observed for the sulfur and selenium derivatives are consistent with the higher polarizability of heavier chalcogens, which facilitates excited-state delocalization without fundamentally altering the nature of the optical transition.

3.1.6. Natural bond orbital and intramolecular hydrogen bonding analysis. To elucidate the electronic nature of the intramolecular hydrogen bonding involved in ESIPT, combined natural bond orbital (NBO), natural population analysis (NPA) and Atoms-in-molecules (AIM) analyses were carried out. The second-order perturbation NBO results (Table S3 of SI) show that the stabilization energy associated with the LP(N) → σ^*(X–H) interaction in the S_0 enol forms decreases from 5.55 kcal mol^{-1} for 8QBDY-O to 5.41 kcal mol^{-1} for 8QBDY-S and 4.39 kcal mol^{-1} for 8QBDY-Se, indicating a progressive weakening of the ground-state hydrogen bond upon replacement of oxygen by heavier chalcogens. This trend reflects the reduced σ*(X–H) acceptor ability arising from the lower electronegativity of sulfur and selenium.

Natural population analysis (Table S4 of SI) supports this interpretation. In the S_0 enol forms, the hydrogen atom bonded to oxygen carries a much higher positive charge (0.499 e) than in the sulfur (0.181 e) and selenium (0.130 e) analogues, evidencing stronger X–H bond polarization in the oxygen

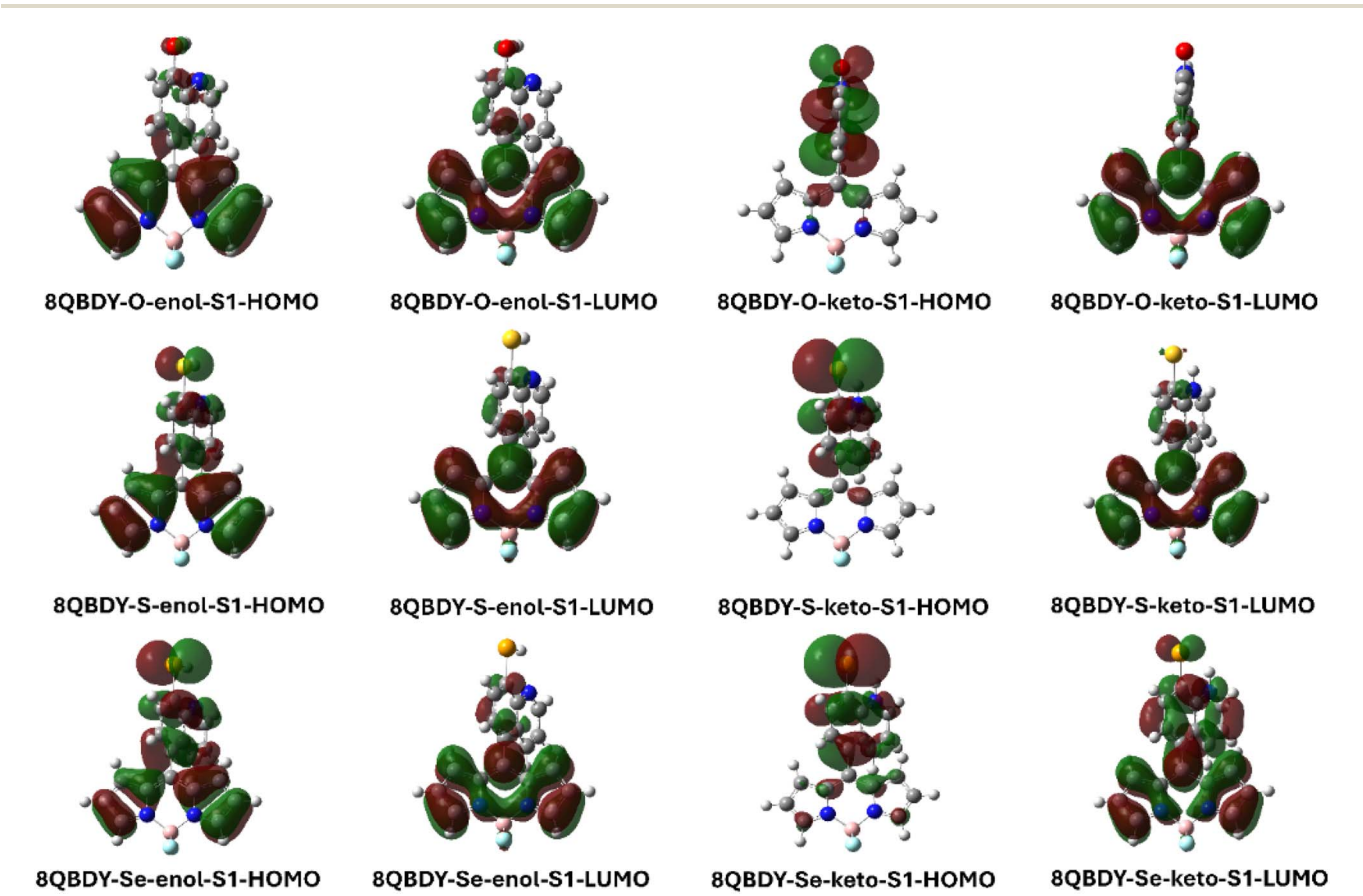

Fig. 7 HOMO and LUMO surfaces of neutral forms of 8-chalcogen-quinoline-BODIPY at the excited state. (Isovalue = 0.02).

derivative. The nitrogen atom remains consistently negatively charged (−0.491 to −0.510 e), confirming its role as the proton-accepting site. Upon excitation to the S_1 state, only minor charge changes are observed for the enol forms, whereas the keto* forms exhibit pronounced charge redistribution, characterized by a more positively charged transferred hydrogen (0.443–0.463 e) and a reduced negative charge on the protonated nitrogen, consistent with N–H bond formation following ESIPT.

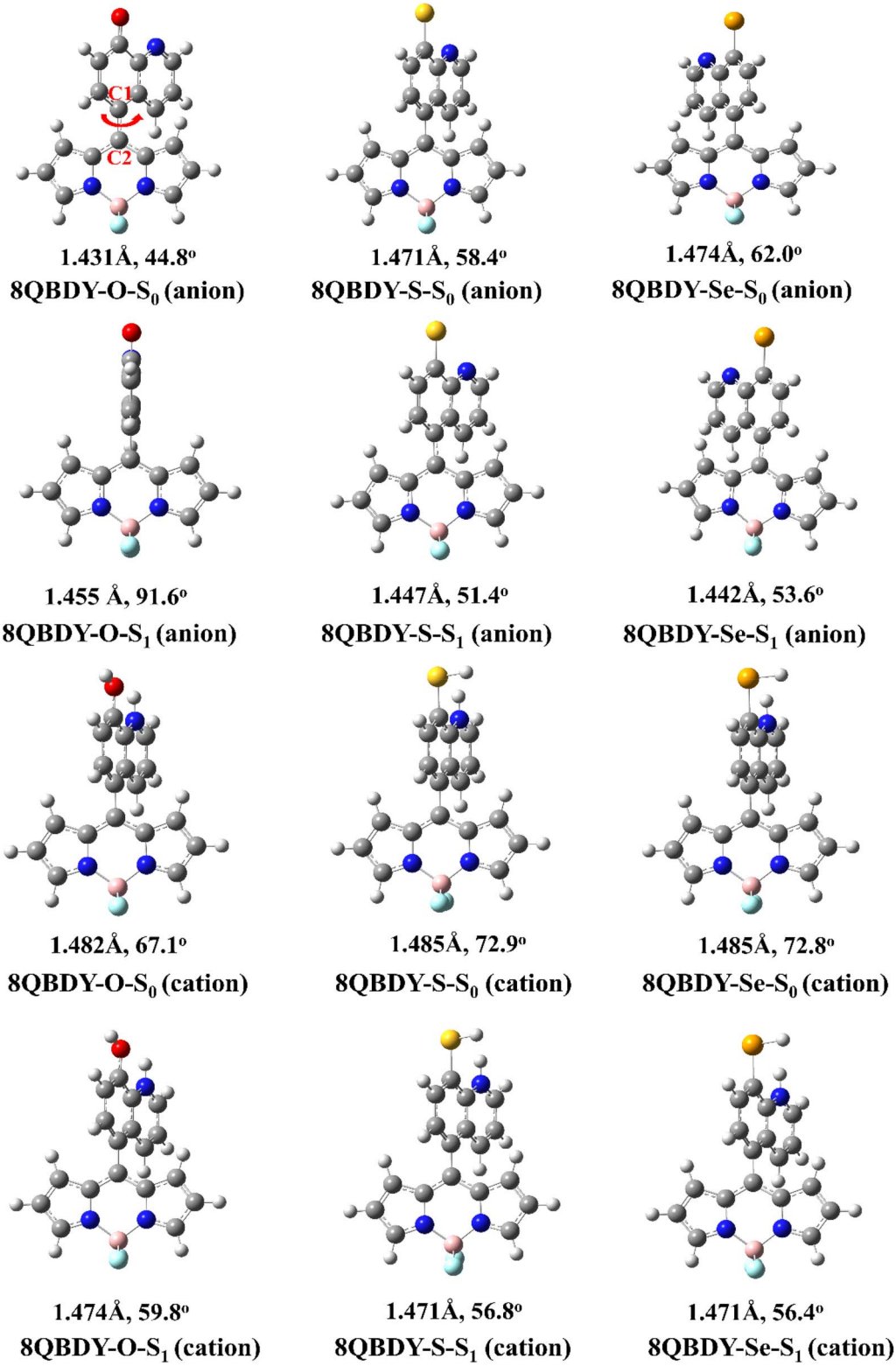

Fig. 8 Optimized structures of protonation/deprotonation of 8-chalcogen-quinoline-BODIPY in ground and excited states.

The AIM analysis (Table S5 and Fig. S4 of SI) further corroborates these trends. For the enol forms, the electron density at the hydrogen-bond critical point decreases from O to Se ($\rho(r) = 0.0257$–0.0204 au), with positive Laplacians and $G(r)/|V(r)|$ ratios greater than unity, characteristic of closed-shell hydrogen bonds. The corresponding hydrogen-bond energies follow the same order ($-6.33 < -4.68 < -3.87$ kcal mol^{-1}). In the S_1 keto* forms, new X···H–N bond paths are identified for the sulfur and selenium derivatives, with moderate electron densities (0.0171–0.0186 au), indicating stabilization of the proton-transferred structures in the excited state.

Collectively, the combined NBO, NPA and AIM results consistently show that heavier chalcogen substitution weakens the ground-state intramolecular hydrogen bond, while ESIPT induces substantial electronic redistribution and stabilization of the keto* tautomer in the excited state.

3.2. Structural and spectroscopic properties of protonation/deprotonation forms

3.2.1. Electron structure characteristics, Wiberg bond indices and dipole moment analysis. The influence of chalcogen substitution on the geometry of protonated and deprotonated 8QBDY-O, 8QBDY-S, and 8QBDY-Se was examined in both S_0 and S_1 states (Fig. 8).

For the cationic forms, all systems display elongated C1–C2 bonds (1.482–1.485 Å) and large dihedral angles (67–73°) in S_0, consistent with weakened π-conjugation due to proton-induced charge localization. Excitation to S_1 shortens the C1–C2 bond (1.474–1.471 Å) and reduces the dihedral angle (59.8–56.4°), indicating enhanced planarity and partial π-delocalization.

For deprotonation forms, the S and Se analogues exhibit typical planarization in S_1, with shorter bonds (1.447 and 1.442 Å) and smaller angles (51.4° and 53.6°), favoring intramolecular conjugation. In contrast, the O derivative behaves anomalously: its C1–C2 bond length increases to 1.455 Å and the dihedral angle expands to 91.6°, producing a strongly twisted geometry that disrupts π-conjugation between quinoline and BODIPY units.

To further elucidate the electronic effects of protonation/deprotonation and chalcogen substitution, Wiberg bond indices (WBI) and dipole moments were analyzed. As shown in Table S6 of SI, the C1–C2 WBI serves as a sensitive probe of π-conjugation between the quinoline and BODIPY units. For the anionic forms, 8QBDY-O exhibits a pronounced decrease in WBI upon excitation (1.222 in S_0 to 1.016 in S_1), indicating loss of π-bond character consistent with the strongly twisted S_1 geometry. In contrast, the sulfur and selenium derivatives show increased WBI values in S_1 (from 1.044 to 1.119 for S and from 1.035 to 1.129 for Se), reflecting enhanced π-delocalization associated with excited-state planarization. For the cationic forms, WBI values remain close to unity (0.996–1.022) in both states, suggesting that protonation induces charge localization and limits further modulation of conjugation.

Dipole moment analysis (Table S6 of SI) provides complementary insight into charge redistribution. The anionic species display much larger dipole moments than the cationic ones, indicating stronger charge separation upon deprotonation. Upon excitation, 8QBDY-*O*-anion shows a notable increase in dipole moment ($\Delta\mu = 4.535$ D), whereas negative $\Delta\mu$ values are obtained for the sulfur (−3.302 D) and selenium (−4.136 D) analogues, consistent with excitation-induced charge localization in the oxygen derivative but enhanced delocalization in the heavier chalcogen systems. By contrast, only minor dipole moment changes are observed for the cationic forms ($\Delta\mu$ = 0.252–0.425 D), indicating limited electronic reorganization.

Overall, the combined WBI and dipole moment analyses demonstrate that heavier chalcogen substitution promotes excited-state π-delocalization and moderates charge separation, whereas the oxygen analogue is more susceptible to excitation-induced conjugation disruption, in agreement with the observed geometric and photophysical trends.

3.2.2. Absorption and emission properties. The absorption and fluorescence properties of the protonated and deprotonated forms of 8QBDY-O, 8QBDY-S, and 8QBDY-Se were examined to clarify how acid–base equilibrium influences their excited-state dynamics (Table 3 and Fig. S5). The results reveal two distinct emission mechanisms: a PeT-controlled ON/OFF fluorescence in the oxygen analogue and dual locally excited (LE) and intramolecular charge-transfer (ICT) emissions in the sulfur and selenium analogues.

For 8QBDY-O, the protonated cation absorbs at 422 nm (f = 0.5582) and emits strongly at 480 nm (f = 0.7085), corresponding to a PeT-inhibited ON state.[23] Protonation reduces the donor capacity of the quinoline nitrogen, suppressing electron transfer and maintaining efficient fluorescence. However, for deprotonation, the anionic form absorbs at 547 nm (f = 0.4811) but exhibits quenched fluorescence (OFF state).[23] The pronounced geometric twisting of the deprotonated O–BODIPY (dihedral angle = 91.6°) disrupts π-conjugation between the quinoline and BODIPY units, facilitating PeT-driven non-radiative decay and emission loss.

Table 3 The absorption and fluorescence spectra of protonation/deprotonation forms of 8QBDY-O, 8QBDY-S and 8QBDY-Se

Compounds	$\lambda_{Abs.}$ (nm)	f (oscillator strengths)	$\lambda_{Flu.}$ (nm)	f (oscillator strengths)	Stokes shifts
8QBDY-*O*-anion	547	0.4811	OFF		
8QBDY-*O*-cation	422	0.5582	480	0.7085	58
8QBDY-S -anion	513	0.301	656	0.6425	143
8QBDY-S -cation	423	0.5646	488	0.6926	65
8QBDY-Se-anion	510	0.2724	660	0.7357	150
8QBDY-Se-cation	423	0.5636	489	0.6913	66

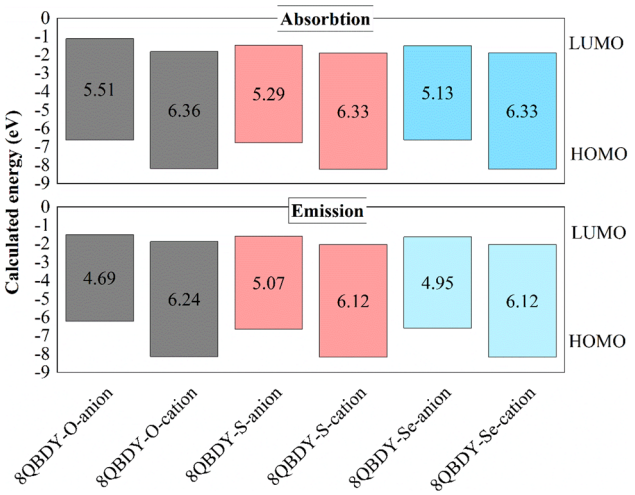

Fig. 9 Energy diagram of HOMO and LUMO levels of absorption/emission of ionic forms of 8-chalcogen-quinoline-BODIPY.

In contrast, the sulfur and selenium derivatives display red-shifted ICT emissions (656–660 nm) with large Stokes shifts (143–150 nm) upon deprotonation, indicating enhanced π-delocalization and charge separation. Thus, while oxygen substitution favors PeT-controlled quenching, heavier chalcogens (S, Se) stabilize near-planar geometries and promote ICT-dominant dual-emission behavior, enabling pH-dependent fluorescence tunability.

3.2.3. Frontier molecular orbitals (MOs), optical band gap (E_{opt}) and exciton binding energy (E_b) analysis. Frontier molecular orbitals (HOMO and LUMO) analysis (Fig. 9 and 10) revealed that both protonation state and chalcogen identity markedly affect the electronic structure of 8QBDY derivatives. For 8QBDY–O, protonation stabilizes the orbitals, producing a wide gap of 6.36 eV (HOMO −8.19 eV; LUMO −1.83 eV), consistent with localized π → π* transitions and strong fluorescence in acidic media (PeT-inactive ON state). Deprotonation raises the HOMO (−6.63 eV) and narrows the gap to 5.51 eV (absorption) and 4.69 eV (emission), enhancing donor strength and facilitating PeT from quinoline to the BODIPY core, leading to fluorescence quenching (OFF state).

In contrast, the S and Se analogues exhibit smaller HOMO–LUMO gaps and distinct ICT-dominant behavior. Protonated forms show deep HOMOs (−8.2 eV) and large gaps (6.3 eV), corresponding to LE-type emissions. Deprotonation elevates the HOMOs (−6.77 eV for S; −6.63 eV for Se) and narrows the gaps (5.29 and 5.13 eV), enhancing π-delocalization and producing strong red-shifted ICT emissions.

As summarized in Table S7 of SI, the cationic forms display relatively large and chalcogen-insensitive E_{opt} values (2.54–2.58

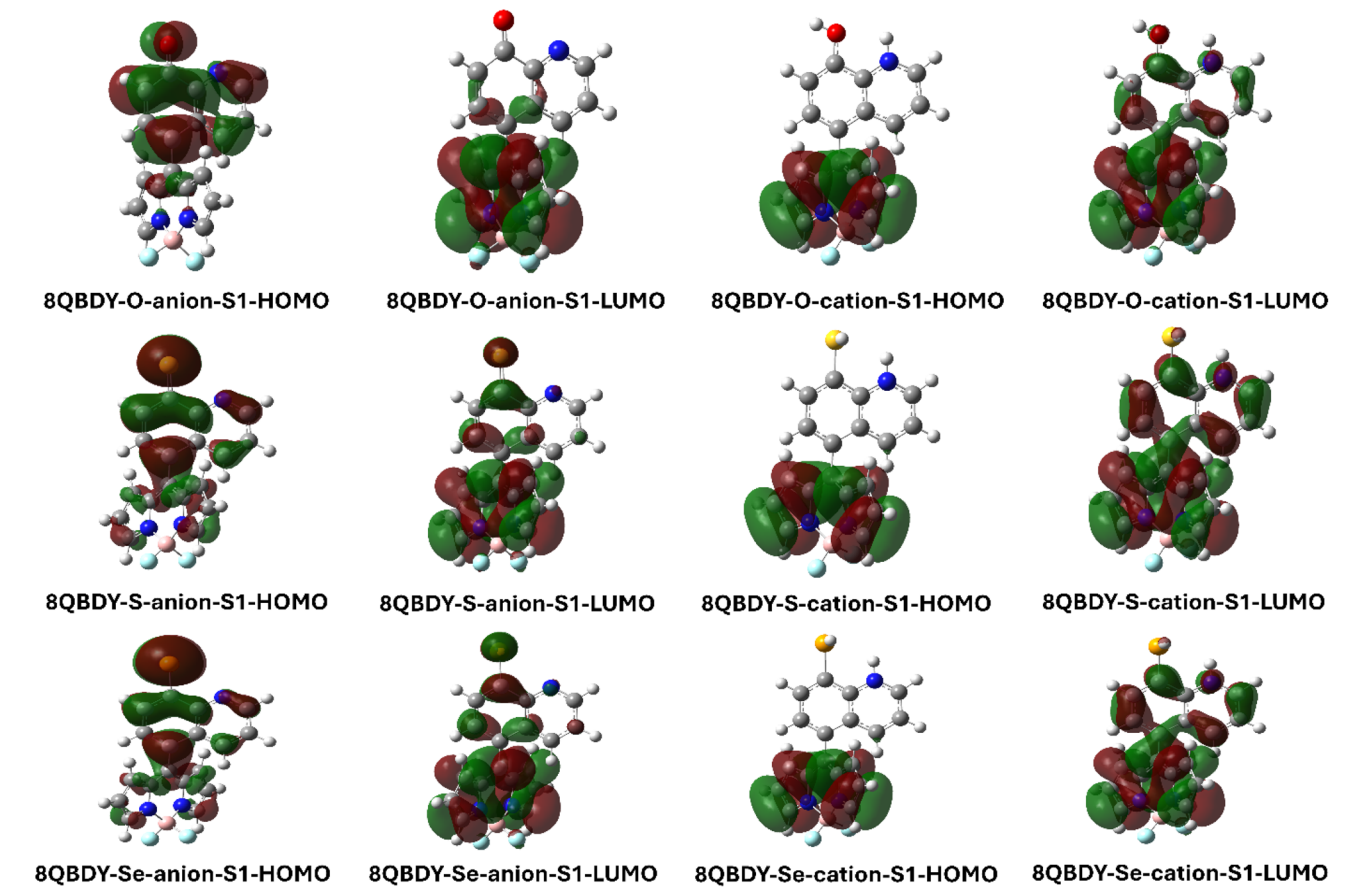

Fig. 10 HOMO and LUMO surfaces of ionic forms of 8-chalcogen-quinoline-BODIPY at excited states. (Isovalue = 0.02).

eV), consistent with wide HOMO–LUMO gaps and predominantly locally excited states. In contrast, deprotonation leads to a pronounced reduction in E_{opt}, most notably for 8QBDY-*O*-anion (1.16 eV), indicating substantial optical gap narrowing associated with enhanced donor strength and activation of PeT/ICT pathways; the sulfur and selenium anions exhibit intermediate E_{opt} values (1.88–1.89 eV), reflecting partial moderation of gap narrowing by improved π-delocalization. The exciton binding energies show a complementary trend: cationic species possess relatively large E_b values (3.58–3.66 eV), indicative of strong electron–hole coulombic attraction, whereas deprotonation reduces E_b to 3.53 eV (O) and further to 3.18 and 3.07 eV for the sulfur and selenium analogues, respectively, consistent with weakened exciton binding due to enhanced charge separation and increased ICT character in the heavier chalcogen systems.

4. Conclusion

In this work, a comprehensive DFT and TD-DFT investigation was performed to elucidate the combined effects of chalcogen substitution (O, S, Se) and ionization on the electronic structure, intramolecular interactions, and fluorescence behavior of 8-chalcogen-quinoline-BODIPY (8QBDY-X) derivatives. The results demonstrate that both the identity of the chalcogen atom and the protonation state play decisive roles in modulating excited-state proton and charge transfer processes.

Geometric, MEP, dipole moment, Wiberg bond index, and NBO/NPA/AIM analyses consistently reveal that replacing oxygen with heavier chalcogens weakens the ground-state intramolecular hydrogen bond while increasing molecular polarizability and electronic flexibility. This combination facilitates proton mobility and stabilizes proton-transferred structures in the excited state, thereby promoting ESIPT. Topological AIM descriptors further suggest the progressive reduction in hydrogen bond strength from O to Se and the formation of stabilized N–H interactions in the excited keto* forms.

Frontier molecular orbital, optical band gap, and exciton binding energy analyses show that protonation stabilizes localized excited states characterized by large electronic and optical gaps and strong electron–hole binding, whereas deprotonation raises the HOMO energy, narrows the gaps, and weakens exciton binding. These changes activate photoinduced electron transfer or intramolecular charge transfer pathways, with sulfur- and selenium-substituted derivatives exhibiting more pronounced ICT character and red-shifted emission compared with the oxygen analogue. For the oxygen-substituted derivative (8QBDY-O), the theoretical predictions qualitatively agree with the experimentally reported ON/OFF fluorescence switching behavior upon protonation/deprotonation.

In summary, this study provides a unified electronic-structure framework linking chalcogen substitution and ionization to ESIPT, PeT, and ICT mechanisms in 8QBDY systems. The insights gained here offer molecular level guidelines for the rational design of BODIPY-based fluorescent probes and sensors with tunable emission behavior through targeted heteroatom substitution and protonation control.

Author contributions

Mai Van Bay: visualization, investigation, formal analysis, data curation, conceptualization. Quan V. Vo: investigation, formal analysis, writing – review & editing, writing – original draft. Nguyen Quang Trung: visualization, validation, investigation, formal analysis, data curation. Nguyen Linh Nam: visualization, validation, investigation, formal analysis, project administration. Pham Cam Nam: methodology, formal analysis, writing – review & editing, supervision. Nguyen Minh Thong: conceptualization, investigation, methodology, formal analysis, writing – original draft, writing – review & editing.

Conflicts of interest

There are no conflicts of interest to declare.

Data availability

The data supporting this article have been included as part of the supplementary information (SI). Supplementary information is available. See DOI: https://doi.org/10.1039/d5ra09145d.

Acknowledgements

This research is funded by the Vietnam Ministry of Education and Training under Grant No. B2025.DNA.02

References

1 A. C. Sedgwick, L. Wu, H. H. Han, S. D. Bull, X. P. He, T. D. James, J. L. Sessler, B. Z. Tang, H. Tian and J. Yoon, *Chem. Soc. Rev.*, 2018, **47**, 8842–8880.
2 P.-Y. Fu, S.-Z. Yi, M. Pan and C.-Y. Su, *Acc. Mater. Res.*, 2023, **4**, 939–952.
3 H. Niu, J. Liu, H. M. O'Connor, T. Gunnlaugsson, T. D. James and H. Zhang, *Chem. Soc. Rev.*, 2023, **52**, 2322–2357.
4 B. Daly, J. Ling and A. P. de Silva, *Chem. Soc. Rev.*, 2015, **44**, 4203–4211.
5 H. Ren, F. Huo, Y. Zhang, S. Zhao and C. Yin, *Sens. Actuators B: Chem.*, 2020, **319**, 128248.
6 H. Sheng, Y. Hu, Y. Zhou, S. Fan, Y. Cao, X. Zhao and W. Yang, *Dyes Pigm.*, 2019, **160**, 48–57.
7 Y. Zhang, J. H. Wang, W. Zheng, T. Chen, Q. X. Tong and D. Li, *J. Mater. Chem. B*, 2014, **2**, 4159–4166.
8 T. Stoerkler, A. D. Laurent, G. Ulrich, D. Jacquemin and J. Massue, *Dyes Pigm.*, 2023, **208**, 110872.
9 P. Zhou and K. Han, *Aggregate*, 2022, **3**, e160.
10 J. E. Kwon and S. Y. Park, *Adv. Mater.*, 2011, **23**, 3615–3642.
11 J. Zhao, S. Ji, Y. Chen, H. Guo and P. Yang, *Phys. Chem. Chem. Phys.*, 2012, **14**, 8803–8817.
12 H. Sunahara, Y. Urano, H. Kojima and T. Nagano, *J. Am. Chem. Soc.*, 2007, **129**, 5597–5604.
13 I. S. Yadav and R. Misra, *J. Mater. Chem. C*, 2023, **11**, 8688–8723.
14 S. G. Awuah and Y. You, *RSC Adv.*, 2012, **2**, 11169.
15 A. Loudet and K. Burgess, *Chem. Rev.*, 2007, **107**, 4891–4932.

16 E. Fron, E. Coutiño-Gonzalez, L. Pandey, M. Sliwa, M. Van der Auweraer, F. C. De Schryver, J. Thomas, Z. Dong, V. Leen, M. Smet, W. Dehaen and T. Vosch, *New J. Chem.*, 2009, **33**, 1490.
17 L. Song, X. Meng, J. Zhao, H. Han and D. Zheng, *Spectrochim. Acta A*, 2022, **264**, 120296.
18 C. Li, M. Hou, J. Jiang, J. Zhao and L. Fan, *Chem. Phys. Lett.*, 2024, **836**, 141035.
19 D. Yang, C. Liu, M. Zhang and J. Zhao, *Molecules*, 2024, 29.
20 L. Jiang, J. Chen, Y. Zhao, L. Zhang, Y. Wang and J. Zhao, *Mol. Phys.*, 2025, **123**, e2441386.
21 M. Chemek, M. Ben Braiek, I. Rosenbusch, F. Rizzo, N. Wazzan, A. Hafiane and K. Alimi, *Opt. Mater.*, 2024, **157**, 116104.
22 M. Chemek, F. I. H. Rhouma, M. Chemek, Z. Safi, A. Kadi, S. Naili, N. Wazzan and A. Kamel, *J. Mol. Model.*, 2024, **30**, 271.
23 J. Borah, A. Rahman, A. Baruah, P. Dutta and P. Khakhlary, *J. Photochem. Photobiol. A*, 2023, **437**, 114423.
24 Y. Chen, H. Wang, L. Wan, Y. Bian and J. Jiang, *J. Org. Chem.*, 2011, **76**, 3774–3781.
25 S. C. Lan and Y. H. Liu, *Spectrochim. Acta A*, 2015, **139**, 49–53.
26 G. Yaermaimaiti, H. An, A. Kadir, X. Rao, C. Qin, B. Abulimiti and M. Xiang, *Results Chem.*, 2024, **7**, 101318.
27 F. Zhang, J. Zhao and C. Li, *J. Phys. Org. Chem.*, 2021, **34**, e4257.
28 C. H. Wang, Z. Y. Liu, C. H. Huang, C. T. Chen, F. Y. Meng, Y. C. Liao, Y. H. Liu, C. C. Chang, E. Y. Li and P. T. Chou, *J. Am. Chem. Soc.*, 2021, **143**, 12715–12724.
29 C. Adamo and D. Jacquemin, *Chem. Soc. Rev.*, 2013, **42**, 845–856.
30 A. D. Laurent, C. Adamo and D. Jacquemin, *Phys. Chem. Chem. Phys.*, 2014, **16**, 14334–14356.
31 A. Schlachter, A. Fleury, K. Tanner, A. Soldera, B. Habermeyer, R. Guilard and P. D. Harvey, *Molecules*, 2021, **26**, 1780.
32 P. D. Anderson and D. M. Hercules, *Anal. Chem.*, 1966, **38**, 1702–1709.
33 E. Y. Silin', V. K. Bel'skii, A. I. Stash, Y. V. Ashaks, L. Y. Pech, D. E. Zaruma and Y. A. Bankovskii, *Russ. J. Inorg. Chem.*, 2006, **51**, 57–63.
34 M. J. Frisch, G. W. Trucks, H. B. Schlegel, G. E. Scuseria, M. A. Robb, J. R. Cheeseman, G. Scalmani, V. Barone, B. Mennucci, G. A. Petersson, H. Nakatsuji, M. Caricato, X. Li, H. P. Hratchian, A. F. Izmaylov, G. Z. J. Bloino, J. L. Sonnenberg, M. Hada, M. Ehara, K. Toyota, R. Fukuda, J. Hasegawa, M. Ishida, T. Nakajima, Y. Honda, O. Kitao, H. Nakai, T. Vreven, J. A. Montgomery, J. E. Peralta, F. Ogliaro, M. Bearpark, J. J. Heyd, E. Brothers, K. N. Kudin, V. N. Staroverov, T. Keith, R. Kobayashi, J. Normand, K. Raghavachari, A. Rendell, J. C. Burant, S. S. Iyengar, J. Tomasi, M. Cossi, N. Rega, J. M. Millam, M. Klene, J. E. Knox, J. B. Cross, V. Bakken, C. Adamo, J. Jaramillo, R. Gomperts, R. E. Stratmann, O. Yazyev, A. J. Austin, R. Cammi, C. Pomelli, J. W. Ochterski, R. L. Martin, K. Morokuma, V. G. Zakrzewski, G. A. Voth, P. Salvador, J. J. Dannenberg, S. Dapprich, A. D. Daniels, O. Farkas, J. B. Foresman, J. V. Ortiz, J. Cioslowski and D. J. Fox, *Gaussian*, 2016.
35 V. Barone and M. Cossi, *J. Phys. Chem. A*, 1998, **102**, 1995–2001.
36 S. J. Akram, S. Meißner and S. Kümmel, *Adv. Funct. Mater.*, 2025, 2419236.
37 S. Kashani, J. J. Rech, T. Liu, K. Baustert, A. Ghaffari, I. Angunawela, Y. Xiong, A. Dinku, W. You, K. Graham and H. Ade, *Adv. Energy Mater.*, 2023, **14**, 2302837.
38 A. Sugie, K. Nakano, K. Tajima, I. Osaka and H. Yoshida, *J. Phys. Chem. Lett.*, 2023, **14**, 11412–11420.
39 B. T. G. Lutz, M. H. Langoor and J. H. van der Maas, *Vib. Spectrosc.*, 1998, **18**, 111–121.
40 N. Prabavathi, A. Nilufer and V. Krishnakumar, *Spectrochim. Acta A*, 2013, **114**, 449–474.
41 E. Deniz, J. M. Schmidt-Engler, K. Ulrich, M. Oberle, G. Wille and J. Bredenbeck, *J. Chem. Phys.*, 2022, **157**, 135102.
42 A. Benidar, B. Khater, J. C. Guillemin, J. A. Gamez and M. Yanez, *J. Phys. Chem. A*, 2009, **113**, 12857–12863.
43 Y. Ling, W. C. Xie, G. K. Liu, R. W. Yan, Y. Wu and J. Tang, *Sci. Rep.*, 2016, **6**, 31981.
44 B. J. Miller, D. L. Howard, J. R. Lane, H. G. Kjaergaard, M. E. Dunn and V. Vaida, *J. Phys. Chem. A*, 2009, **113**, 7576–7583.
45 J. A. Gomez Castano, R. M. Romano, H. Beckers, H. Willner, R. Boese and C. O. Della Vedova, *Angew. Chem.*, 2008, **47**, 10114–10118.
46 N. Boens, V. Leen and W. Dehaen, *Chem. Soc. Rev.*, 2012, **41**, 1130–1172.
47 A. Kukoyi, H. He and K. Wheeler, *J. Photochem. Photobiol. A*, 2022, **425**, 113686.
48 J. Chen and J. Zhao, *RSC Adv.*, 2024, **14**, 26133–26141.
49 D. Yang and Y. Yang, *Spectrochim. Acta A*, 2024, **313**, 123926.
50 A. Bourouina, M. Rekhis and M. Trari, *Polyhedron*, 2017, **127**, 217–224.